

Effects of Resolution and Local Stability on Galactic Disks: 2. Halo Resolution and Softening on Bar Formation

S. Kwak¹, I. Minchev¹, M. Steinmetz^{1,2}, and S. K. Yi³

¹ Leibniz-Institut für Astrophysik Potsdam (AIP), An der Sternwarte 16, 14482, Potsdam, Germany
e-mail: skwak@aip.de

² Universität Potsdam, Institut für Physik und Astronomie, Karl-Liebknecht-Str. 24-25, 14476, Potsdam, Germany

³ Department of Astronomy and Yonsei University Observatory, Yonsei University, Seoul, 03722, Republic of Korea

March 4, 2026

ABSTRACT

Using N-body simulations, we examine the impact of dark matter (DM) halo resolution and gravitational softening on bar formation. We generate isolated disk-halo systems with fixed stellar disk parameters, varying the number of halo particles, softening lengths, and halo concentration to modulate disk stability via the central DM fraction. The effects of DM resolution ($m_{\text{DM}}/m_{\star} = 1, 10, \text{ and } 100$) on bar formation are less pronounced in more unstable disks, in which the overall evolutionary path is similar except that the lowest DM resolution model suffers gradual bar weakening. Irrespective of the halo resolution, large softening, ϵ_{DM} , flattens the central halo density profile within the softening scale, impeding angular momentum transfer to the nascent bar and preventing bar formation in more stable models. In unstable models with $\epsilon_{\text{DM}} = 0.96$ kpc, a small bar still emerges due to enhanced initial instability and a larger seed perturbation, yet its strength remains capped at $F_2 \approx 0.3$ owing to unresolved central dynamical friction. Despite the destabilizing effect of reduced central DM fractions, our results indicate that deficient central angular momentum exchange can still suppress bar growth. Furthermore, halo softening influences buckling instability, as larger values ($\epsilon_{\text{DM}} = 0.30$ and 0.60 kpc) inhibit central vertical heating, exacerbating radial-vertical velocity dispersion anisotropies and triggering stronger buckling.

Key words. Galaxies: spiral – Galaxies: evolution – Galaxies: kinematics and dynamics – Galaxies: structure

1. Introduction

Numerical effects, including particle numbers and gravitational softening lengths, has long posed challenges in galaxy simulations by introducing artifacts that bias outcomes beyond physical effects (Athanasoula & Sellwood 1986; White 1988; Hernquist & Barnes 1990; Pfenniger & Friedli 1993; Romeo 1994; Merritt 1996; Weinberg 1996; Romeo 1997, 1998). To reduce the numerical noises, different techniques (e.g., wavelet) have been proposed (Romeo et al. 2003, 2004). Among early studies on two-body relaxation, Steinmetz & White (1997) demonstrated that discreteness effects from massive dark matter (DM) particles cause spurious heating of baryons. It overwhelms radiative cooling when DM particle masses exceed critical thresholds and leads to artificial gas expansion or suppressed cooling. Later, Moore et al. (1999) and Fukushige & Makino (2001) showed in the simulations of DM halo formation that larger softening values produce shallower central densities, emphasizing the need for sufficient resolution to preserve cuspy profiles instead of flattened cores. Similarly, Power et al. (2003) stressed that convergence in halo profiles requires precise tuning of softening, time steps, force accuracy, initial redshifts, and particle counts; poor choices yield artificially low central densities or spurious cusps, as softening imposes a characteristic acceleration that must align with orbital timescales and enclosed particles to prevent collisional dominance. Rodionov & Sotnikova (2005) also conducted convergence tests on optimal softening criteria and suggested that softening lengths should be 1.5–2 times smaller than interparticle distances in dense regions to minimize

irregular forces and maintain equilibrium in collisionless models like Plummer or Hernquist spheres.

Recent studies have demonstrated how numerical artifacts, especially from low mass resolution and high DM-to-baryon particle mass ratios, significantly affect galaxy morphologies and properties in idealized and cosmological simulations. For example, energy equipartition in setups with ratios > 1 causes spurious kinetic energy transfer from DM to baryons, artificially enlarging galaxy sizes (Ludlow et al. 2019). Related research on stellar disc heating shows collisional effects from coarse DM particles raise vertical and radial velocity dispersions, thickening and expanding discs across all radii, with severity inversely proportional to DM particle count and pronounced for halos with $\lesssim 10^6$ particles (Ludlow et al. 2021). Here, spurious dispersions can surpass 10% of the halo’s virial velocity over a Hubble time, interfering thin disk properties in Milky Way-mass systems. In full cosmological contexts, these heating artifacts produce resolution-dependent divergences in kinematics and structures, yielding hotter stellar discs, colder halos, elevated central DM densities, and oversized galaxies, while under-resolving dwarf halos suppresses substructure and mergers (Ludlow et al. 2023). Hence, even in the modern simulation era, the numerical setup must be assigned carefully.

Considering all these numerical effects, conducting large-scale cosmological simulations with star formation and feedback to form realistic galaxies remains challenging, particularly for the formation of non-axisymmetric structures and their evolution over the Hubble time (Grand et al. 2017; Pillepich et al. 2018b,a, 2019; Libeskind et al. 2020; Dubois et al. 2021; Ansar et al. 2025). Among them, the NEWHORIZON simulation (Dubois et al.

2021) may be exposed to greater numerical effects as their DM particle mass is about 92 times more massive than baryonic particles. In fact, the bar instability in disks is sensitive to galaxy size, mass, thickness, and kinematics (Fall & Efstathiou 1980; Efstathiou et al. 1982; Athanassoula 2003; Klypin et al. 2009; Kwak et al. 2017), while those properties are sensitive to the DM resolution effects. Moreover, the gravitational softening may affect the angular momentum exchange, while the history of angular momentum exchange via DM-star dynamical interactions directly influences the evolution of bar properties such as bar strength, length, pattern speed, buckling instability, and overall morphology (Athanassoula 2002, 2003, 2014; Berentzen et al. 2006; Jang & Kim 2024; Jang et al. 2025; Kwak et al. 2017, 2019; Łokas et al. 2014, 2016; Łokas 2019a,b, 2025a,b; Martinez-Valpuesta & Shlosman 2004; Martinez-Valpuesta et al. 2006).

Indeed, Kaufmann et al. (2007) showed that angular momentum transport, disk morphology, and radial profiles depend critically on force and mass resolution, with large softening suppressing bar instability. Such excessive softening ($\epsilon = 2$ kpc for both baryon and DM particles) fails to resolve the central region, where angular momentum transport plays a pivotal role in forming a bar. As Bekki (2023) demonstrated, a weak seed bar ($F_2 < 0.1$) initially forms through apsidal precession synchronization (APS), subsequently growing via APS; this seed forms more rapidly under conditions of higher disk mass or strong tidal perturbations. However, adopting large softening lengths and lower DM resolution is expected to reduce angular momentum transfer, especially during the early growth phase when the bar is small as originating from the very center. In Kwak et al. (2025) (Paper I), we emphasized the role of central angular momentum exchange in mediating the transition from the spiral phase to the bar phase. In a fixed potential halo, in which the angular momentum exchange is absent, this transition does not happen, thereby suppressing bar formation in models with the same disk stability. Thus, poorly resolving central dynamics between DM and star by a low number of particle and a large choice of softening is expected to alter the bar instability, as observed in the NEWHORIZON simulation (Reddish et al. 2022).

In this paper, we investigate the effects of resolution and gravitational softening length in the DM halo on bar formation and evolution in idealized disk-halo models. All models employ identical stellar disk parameters, allowing us to isolate their numerical influences. By varying the DM concentration, we compare the relative impacts of different disk stabilities on bar formation and long-term growth. Furthermore, by examining numerical effects on vertical heating, we assess how buckling instability strength varies with resolution and softening. In Section 2, we list our numerical setup, including the disk-halo models, halo structure, and N -body code. Section 3 presents an overview of bar evolution as diverged by resolution and softening—both in combination and separately—and visualizes the occurrence of buckling instability under different softening lengths. In Section 4, we discuss the underlying physical mechanisms, linking our findings to similar studies and cosmological simulations. We conclude Section 4 with recommendations on appropriate choices for resolution and softening.

2. Numerical Setup

2.1. Initial Conditions

We construct the initial conditions in the same manner as in Paper I using the GALIC code (Yurin & Springel 2014). Our

Table 1: Initial Conditions

Model	c	N_{DM}	m_{DM}/m_{\star}	ϵ_{DM} [kpc]
r1c16	16	1.14e7	10	0.03
r1c16ldm	16	1.14e6	100	0.03
r1c16ldmsf06	16	1.14e6	100	0.60
r1c16ldmsf1	16	1.14e6	100	0.96
r1c16sf1	16	1.14e7	10	0.96
r1c14	14	1.14e7	10	0.03
r1c14ldm	14	1.14e6	100	0.03
r1c14ldmsf06	14	1.14e6	100	0.60
r1c14ldmsf1	14	1.14e6	100	0.96

Notes. Column (1) is the model name. Column (2) is the halo concentration. Columns (3) and (4) are the total number of DM halo particles, and the mass ratio between DM and star particle. The last column is the gravitational softening for DM particles.

galaxy models consist of a disk-halo system in isolation. The stellar disk follows the distribution

$$\rho_{\star}(R, z) = \frac{M_d}{4\pi z_d R_d} \exp\left(-\frac{R}{R_d}\right) \text{sech}^2\left(\frac{z}{z_d}\right), \quad (1)$$

where R_d is the scale length, z_d is the vertical scale height, and M_d is the total mass of the stellar disk in cylindrical coordinates. In all models, the parameters for the stellar disk are the same: $M_d = 5 \times 10^{10} M_{\odot}$, $R_d = 3$ kpc, and $z_d = 0.3$ kpc. The resolution for the stellar disk is fixed, with $N_{\star} = 5 \times 10^6$ particles, each having a mass of $m_{\star} = 10^4 M_{\odot}$. The softening length of the stellar component ϵ_{\star} is 0.03 kpc, which is the mean particle separation in the disk within the half-mass radius.

The dark matter (DM) halo follows a Hernquist (1990) profile in spherical coordinates

$$\rho_{\text{DM}}(r) = \frac{M_{\text{DM}}}{2\pi} \frac{a}{r(r+a)^3}, \quad (2)$$

where a is the scale length of the halo and M_{DM} is the total mass. The total mass is fixed at $M_{\text{DM}} = 1.14 \times 10^{12} M_{\odot}$ in all models. The scale length of the DM halo varies with the concentration parameter c as

$$a = \frac{r_{200}}{c} \left[2 \ln(1+c) - \frac{c}{1+c} \right]^{1/2}, \quad (3)$$

where r_{200} is the virial radius (Springel et al. 2005). We adopt two halo concentration parameters, $c = 14$ and 16, that fall within the reasonable range from Aquarius and TNG simulations (Springel et al. 2008; Bose et al. 2019). The scale lengths a are 22.88 and 20.68 kpc, respectively. Although we use the same parameters for the stellar disk, varying the halo concentration changes the central fraction of the DM halo, which affects the bar instability of disk galaxies (Kwak et al. 2017, 2019; Jang & Kim 2023). Hence, our models are imposed with two different levels of stability. According to the Toomre Q parameter (Toomre 1964),

$$Q = \frac{\kappa \sigma_R}{3.36 G \Sigma_{\star}}, \quad (4)$$

the corresponding minimum Q values are 0.830 and 0.875 for the ‘c14’ and ‘c16’ models, respectively.

The parameters of our models are listed in Table 1. In each set of our galaxy models with different stability, we vary the resolution and the gravitational softening length of the DM halo.

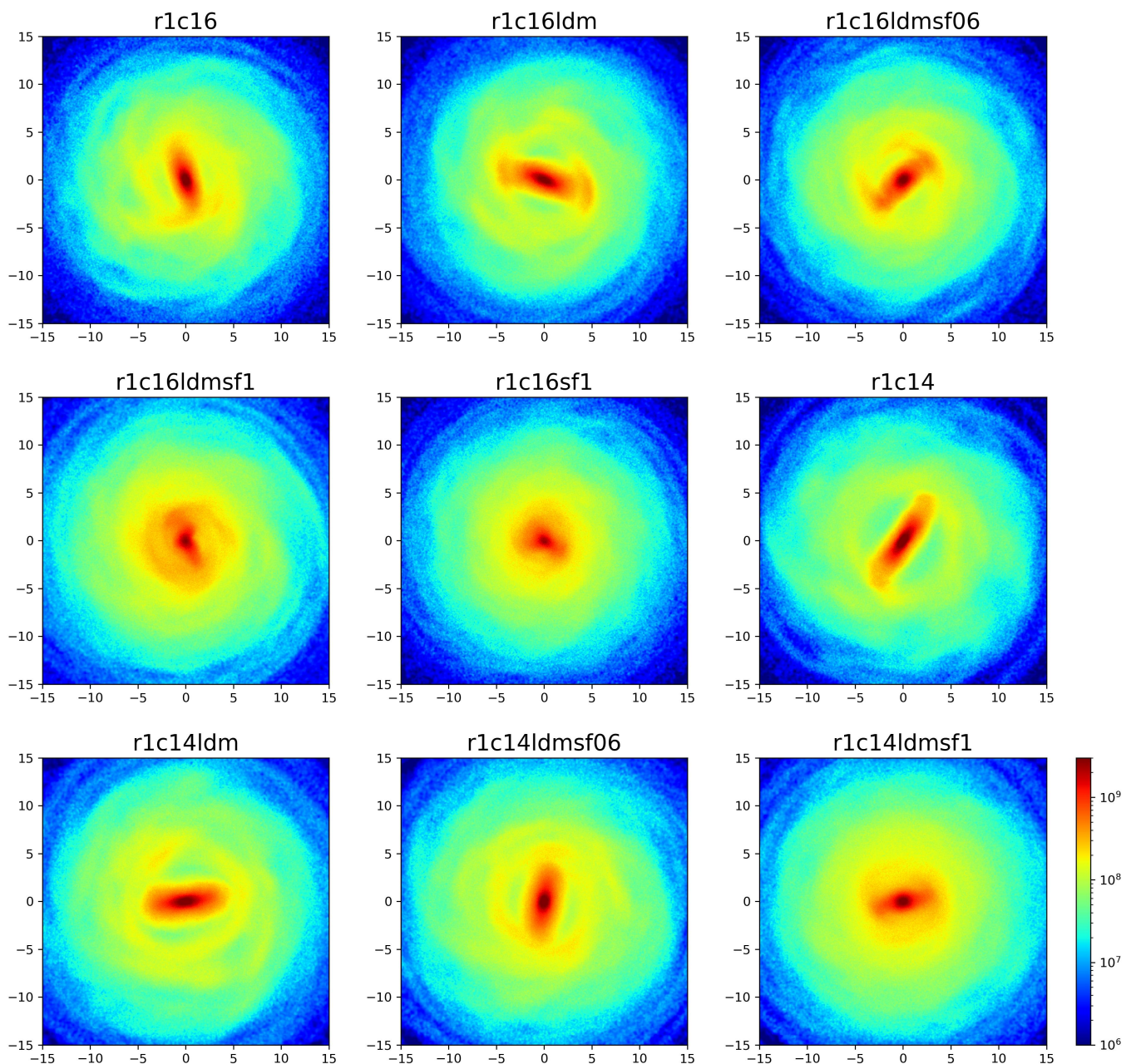


Fig. 1: Face-on projections of stellar surface density distribution in a 30×30 kpc box at 4 Gyr for all models.

The ‘ldm’ models contain $N_{\text{DM}} = 1.14 \times 10^6$ with $m_{\text{DM}}/m_{\star} = 100$, while the rest have $N_{\text{DM}} = 1.14 \times 10^7$ with $m_{\text{DM}}/m_{\star} = 10$. For such galaxies with low DM resolution, large softening is often adopted. We therefore evolve two additional models with $\epsilon_{\text{DM}} = 0.60$ kpc and 0.96 kpc for the ‘c14’ and ‘c16’ models. The value of 0.96 kpc is derived from the mean particle separation within the effective radius of the DM halo in model r1c16ldm, while 0.60 kpc is the mean particle separation within 27 kpc ($9R_d$). We denote models with $\epsilon_{\text{DM}} = 0.96$ kpc and 0.60 kpc as ‘sf1’ and ‘sf06’, respectively. For example, model r1c16ldmsf1 includes a DM halo with $N_{\text{DM}} = 1.14 \times 10^6$, $\epsilon_{\text{DM}} = 0.96$ kpc, and $c = 16$. In the models without ‘sf1’ or ‘sf06’ denotation, the same softening length is assigned for both the disk and halo $\epsilon_{\text{DM}} = 0.03$ kpc.

To examine the softening effects separately, we apply the same large softening in the higher resolution halo in the r1c16sf1

model with $\epsilon_{\text{DM}} = 0.96$ kpc. Additionally, the effects of $\epsilon_{\text{DM}} = 0.30$ kpc and $m_{\text{DM}}/m_{\star} = 1$ are compared in Appendix B after evolving model r1c14ldmsf03 and r1c14hdm. The ‘hdm’ stands for the high DM resolution, which contains 1.14×10^8 DM particles. All models are evolved for 4 Gyr with 400 output snapshots using the AREPO code (Weinberger et al. 2020).

3. Results

3.1. Overview

Figure 1 illustrates the surface density distribution of the stellar disk in all models within a $30 \text{ kpc} \times 30 \text{ kpc}$ box at the end of the simulation (4 Gyr). The ‘c16’ models share the same disk parameters but differ in DM resolution and softening. These differences yield noticeably distinct outcomes. Note that r1c16 is

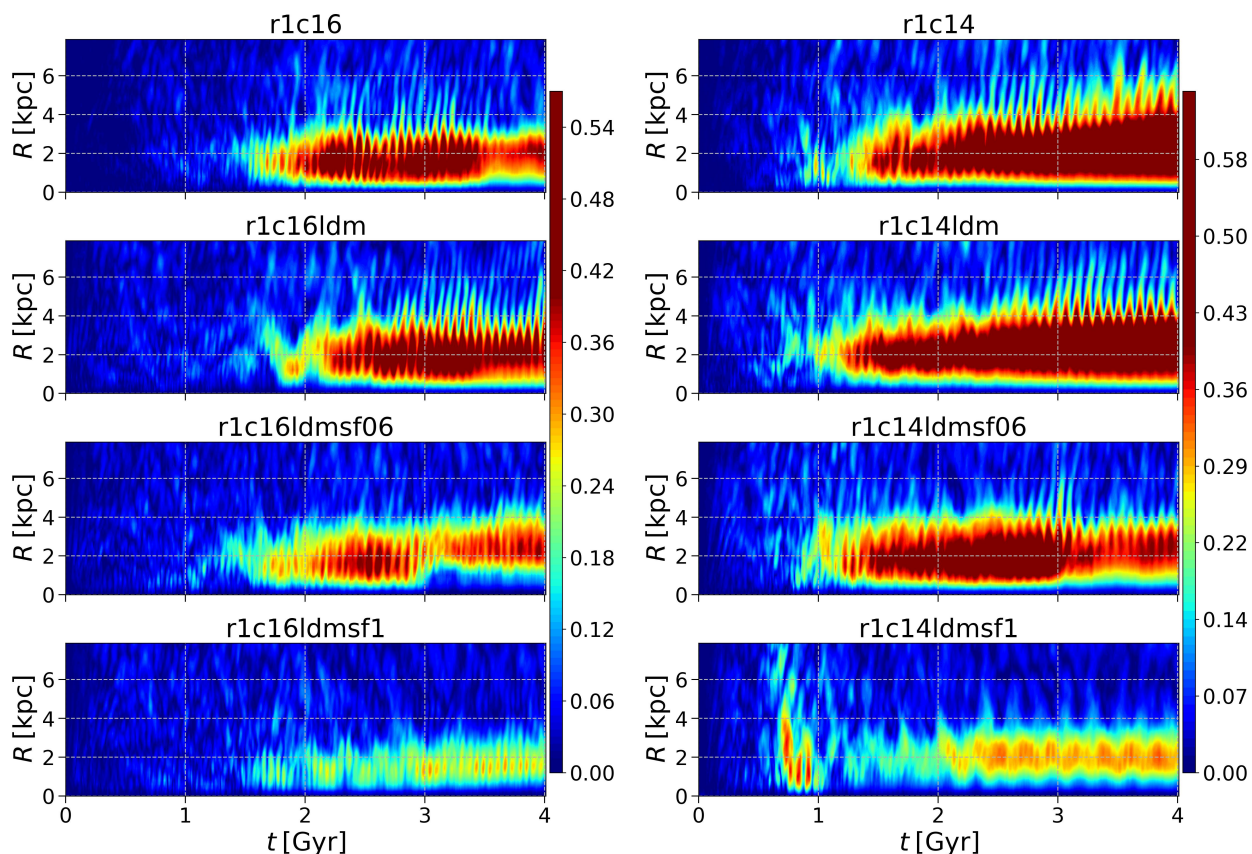


Fig. 2: Fourier map calculated from the time evolution of radial Fourier profiles of $m = 2$ mode within 8 kpc. The time interval is 0.01 Gyr with 400 snapshots for 4 Gyr. The scale of the color bar is fixed from 1% to 40%, so that the same color indicates the same amplitude.

a marginally unstable model in terms of spiral formation, as demonstrated in Paper I. The bar formation epochs of r1c16 and r1c16ldm, based on $F_{2,\max} > 0.3$, are 1.67 Gyr and 1.89 Gyr, respectively. Model r1c16 exhibits a prominent bar at 4 Gyr, as does model r1c16ldm despite its low DM resolution ($m_{\text{DM}}/m_{\star} = 100$). The bar in model r1c16ldmsf06 ($\epsilon_{\text{DM}} = 0.60$ kpc), which has larger softening than r1c16 and r1c16ldm ($\epsilon_{\text{DM}} = 0.03$ kpc), appears slightly weaker. Interestingly, despite the same stability, model r1c16ldmsf1 ($\epsilon_{\text{DM}} = 0.96$ kpc) fails to form an elongated bar even by the end of the simulation. One might conjecture that the resolution of its DM halo prevents bar formation. However, model r1c16sf1, with 10 times more DM particles ($m_{\text{DM}}/m_{\star} = 10$), still does not develop a large-scale bar owing to the large DM softening value ($\epsilon_{\text{DM}} = 0.96$ kpc); only a weak inner oval/short bar is present. This implies that the choice of an excessively large halo softening length, which is often adopted to mask numerical noise in low DM resolution simulations, exerts a greater impact on bar formation and growth.

The stellar disks in the ‘c14’ models are gravitationally more unstable than those in the ‘c16’ models in terms of the Toomre Q parameter. The lower halo concentration parameter in the ‘c14’ models results in a smaller DM contribution within the disk region. This leads to a lower Toomre Q distribution and makes the disks more susceptible to instabilities and the formation of non-axisymmetric structures. In fact, as shown in Paper I, model r1c14 forms a visible bar by surpassing $F_{2,\max} > 0.3$ at 1.26 Gyr. This occurs 0.41 Gyr earlier than in model r1c16 with the same resolution. In Figure 1, model r1c14 forms a well-elongated and

strong bar after evolving for 4 Gyr. In the models with lower resolution or larger softening, the bars tend to be shorter and weaker. Although model r1c16ldmsf1 with $\epsilon_{\text{DM}} = 0.96$ kpc fails to form a bar, model r1c14ldmsf1 does form one. However, this bar appears much smaller than those in the other models. This implies that bar formation and growth depend on the initial disk stability, softening length, and DM halo resolution. In a more unstable disk, a stronger seed bar (e.g., Bekki 2023) can form earlier. We conjecture that this enables bar formation in model r1c14ldmsf1 despite the suppressed bar–halo angular momentum exchange due to the large DM softening. However, the growth of the bar is not fully resolved owing to the suppressed DM response (and thus reduced DM–star dynamical friction) in the central bar region. Consequently, the bar is unable to grow stronger and longer in model r1c14ldmsf1.

3.2. Bar Formation and Growth

To trace the formation and evolution of non-axisymmetric structures, we perform a Fourier analysis:

$$F_0(R) = \sum_j \mu_j, \quad (5)$$

$$F_m(R) = \frac{\sum_j \mu_j e^{im\phi_j}}{F_0(R)}. \quad (6)$$

Here, μ_j and ϕ_j are the mass and azimuthal angle of the j th particle in an annulus with a radial bin width of $\Delta R = 0.2$ kpc. The

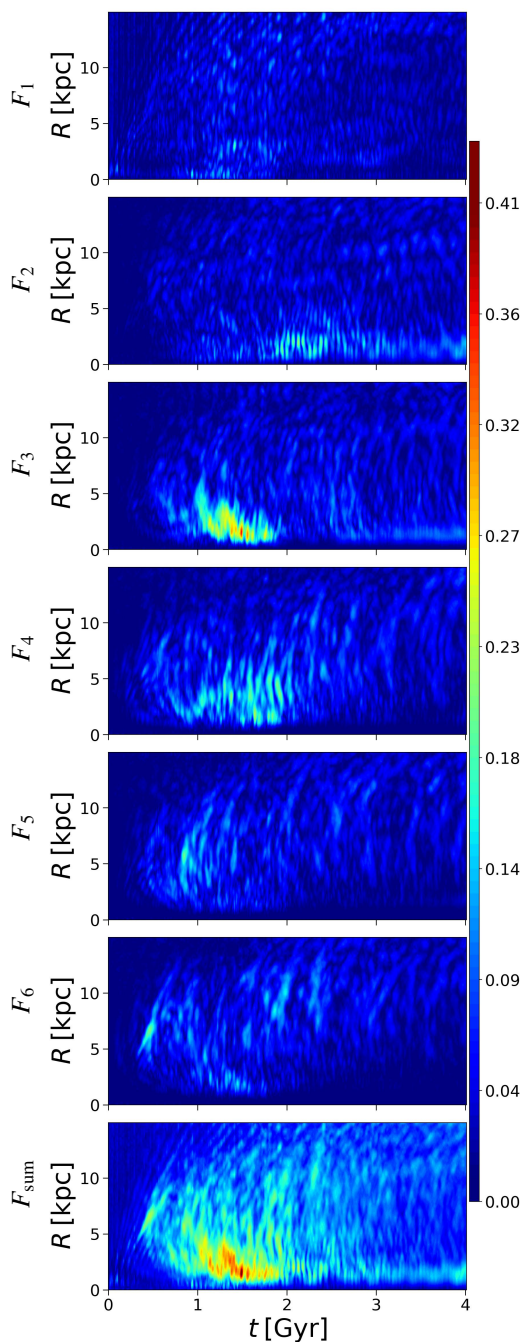


Fig. 3: Fourier contour map calculated from the time evolution of radial Fourier profiles of each mode and F_{sum} in model r1c16sf1. The time interval of each snapshot used is 0.01 Gyr. The color scale of each color bar is fixed from 1% to 40%, so that the same color indicates the same amplitude.

value of m is an integer that denotes the multipole order. We primarily focus on $m = 2$ to quantify the bar strength and examine the evolutionary path of bars.

Figure 2 visualizes the time evolution of the Fourier mode $m = 2$ within 8 kpc over 4 Gyr. The left and right columns correspond to the ‘c16’ and ‘c14’ models, respectively. The scale of the color bar is fixed from 0.01 to 0.40. Red and orange regions indicate strong $m = 2$ non-axisymmetry with $F_2 > 0.3$, which we use as an approximate bar-length proxy. However, near the

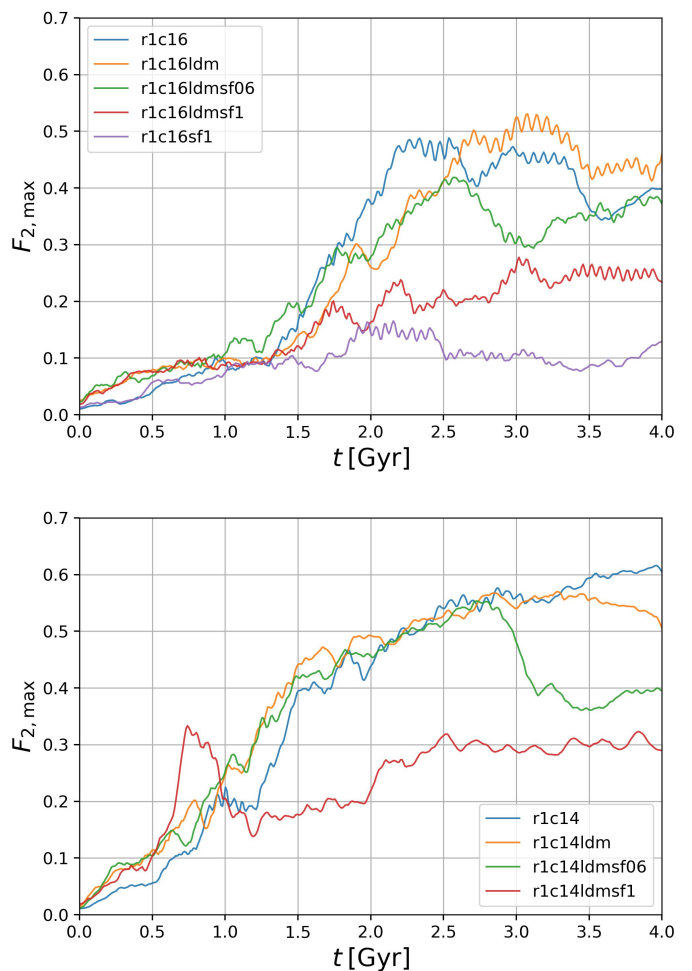


Fig. 4: Time evolution of the maximum value of the Fourier mode $m = 2$ in the ‘c16’ models (top panel) and ‘c14’ models (bottom panel), after smoothing the data by applying a moving average over 9 points.

bar end this threshold can be exceeded during episodes of bar-spiral mode coupling (Minchev & Famaey 2010; Quillen et al. 2011; Hilmi et al. 2020; Marques et al. 2025). In these intervals, because the bar rotates faster than the spiral pattern, it periodically overlaps with the $m = 2$ spiral on the timescale set by their beat frequency. During such alignments the two $m = 2$ components add constructively, boosting F_2 outside the physical bar and thereby increasing the bar’s measurable length in the F_2 map. Depending on the strength of the inner spiral structure, the apparent bar length can be overestimated by up to a factor of ~ 2 , both in stellar surface-density maps (Hilmi et al. 2020) and in the centrally induced quadrupole velocity field (Vislosky et al. 2024). A more conservative length estimate is therefore given by the lower envelope of the $F_2 > 0.3$ boundary (times when the spiral contribution is weakest).

Overall, the differences in bar formation epochs are small among models with the same disk stability in Figure 2. As presented in Paper I, more stable disks are more susceptible to Poisson noise with regard to spiral and bar formation. For instance, increasing the *total* resolution (star and DM) of model r1c16 by a factor of 10 delays bar formation by 1.9 Gyr, whereas the delay is only 0.5 Gyr in model r1c14 with the same resolution enhancement (the ‘r2’ models in Paper I). Additionally, the reso-

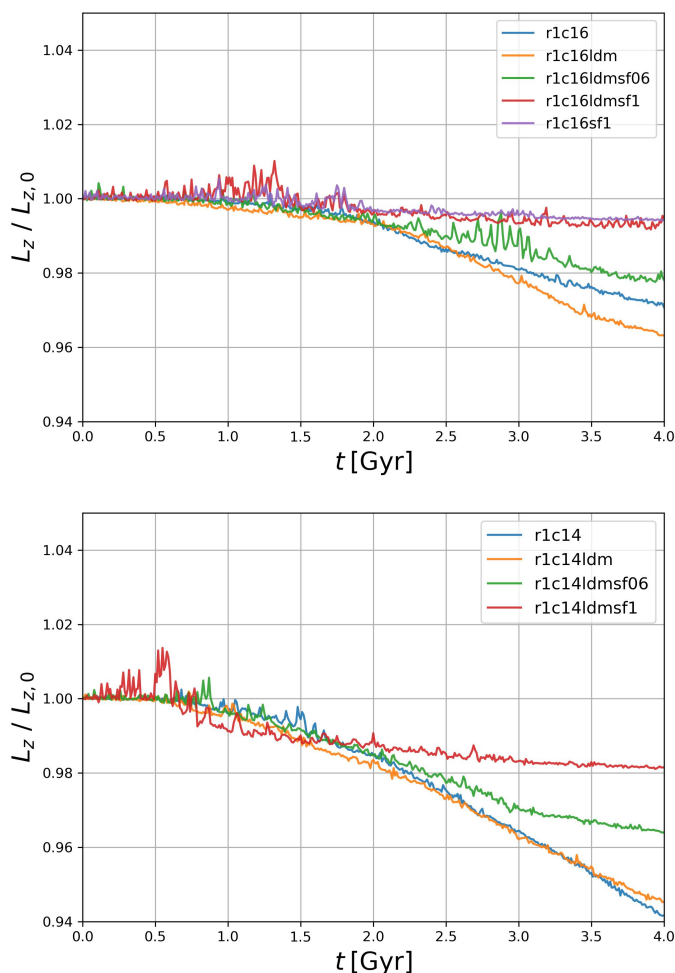


Fig. 5: Time evolution of the disk angular momentum normalized to its initial value, $L_z/L_{z,0}$, over 4 Gyr. The top panel corresponds to the ‘c16’ models, and the bottom panel to the ‘c14’ models.

lution of the DM halo, which is one of the main focuses of this study, slightly delays bar formation as well: (1) decreasing the DM resolution by a factor of 10 (model r1c16ldm) triggers spurious spirals due to massive DM particles, which heat the disk and thus slightly stabilize it; (2) increasing the DM resolution (model r1c16hdm in Paper I) reduces discreteness noise associated with large m_{DM}/m_{\star} , resulting in a smoother transition from the spiral phase to the bar phase. Again, all the models have the same disk resolution in this work. In addition to these resolution effects, varying the DM softening lengths introduces further complexity to the numerical effects and the ensuing bar formation. Still, relative to the case of increasing the total resolution by a factor of 10, these differences driven by softening and DM resolution in bar formation epochs are not significant, except for the ‘sf1’ models with $\epsilon_{\text{DM}} = 0.96$ kpc.

Model r1c16 possesses a small bar at 2 Gyr (Fig. 1 in Paper I), which grows stronger afterward via angular momentum exchange between stars and DM (Athanasoula 2002; Sellwood 2016; Kwak et al. 2017), shown until 4 Gyr in Figure 2. Although the bar formation time delay is only 0.41 Gyr relative to model r1c14, the two models undergo significantly different evolutionary paths in bar formation and growth. Model r1c14 forms the strongest bar among all the models. Model r1c16 forms a

weaker bar and experiences two bar weakening phases around 2.5 Gyr and 3.5 Gyr, due to vertical buckling instability. The bar in model r1c14 grows continuously without experiencing noticeable buckling instability and forms a well-elongated bar with the region of $F_2 > 0.3$ extending to 4 kpc at 4 Gyr, excluding the bar-spiral coupled regions. In terms of length and strength, model r1c14 with $m_{\text{DM}}/m_{\star} = 10$ forms the longest bar. Note that the vertical buckling instability can occur either gradually with a small amplitude in v_z or suddenly with a strong impact in v_z (e.g., Kwak et al. 2017; Seo et al. 2019; Łokas 2020). In the following sections, we refer to the gradual and weak heating as vertical instability and the sudden, strong one as buckling instability.

Decreasing the DM halo resolution while keeping the DM softening the same has no significant effect over the 4 Gyr evolution period in our idealized disk-halo systems. Model r1c16ldm forms a bar slightly later than model r1c16 due to the stabilizing effects from early spiral heating by massive DM particles with $m_{\text{DM}}/m_{\star} = 100$. It also experiences weakening in F_2 around 3.5 Gyr within the central few kpc region, but not as much as r1c16 does. The overall strength and size of the bar are comparable to those in r1c16. When comparing models r1c14 and r1c14ldm, their overall evolutionary paths appear similar, although the bar is slightly shorter at 4 Gyr in model r1c14ldm. There are small differences in minor details when $m_{\text{DM}}/m_{\star} = 10 \rightarrow 100$, but the overall outcomes appear comparable.

At a glance, Figure 2 reveals that DM softening exerts the most dramatic effects on bar formation and growth. As the DM softening length increases ($\epsilon_{\text{DM}} = 0.03 \rightarrow 0.60 \rightarrow 0.96$ kpc), the bar strength visibly decays. In the ‘sf06’ models with $\epsilon_{\text{DM}} = 0.60$ kpc, the bar forms more weakly and the bar-driven spirals noticeably diminish relative to models with $\epsilon_{\text{DM}} = 0.03$ kpc. Furthermore, model r1c14ldmsf06 experiences significant bar weakening around 3 Gyr. Concurrently, bar-driven spirals appear larger temporarily. Note that these spiral structures are distinct from the periodic spirals in other models with $\epsilon_{\text{DM}} = 0.03$ kpc and represent remnants of the buckling instability (see Fig. 8 in Łokas 2019b). During the buckling instability, in addition to vertical thickening and the formation of an X-shaped bulge (linked to the bar’s 2:1 vertical resonance; Quillen et al. 2014), the bar dissolves and shortens, forming the barred spirals by ejecting a fraction of stars from the barred orbits. After the buckling instability, its bar strength remains weak and does not grow stronger as in the pre-buckling phase.

In the ‘sf1’ models, the large DM softening ($\epsilon_{\text{DM}} = 0.96$ kpc) significantly suppresses bar formation (Fig. 2). The bar strength in model r1c16ldmsf1 does not exceed $F_2 = 0.3$. In the face-on views (Fig. 1), this model develops at most a weak/short inner oval, i.e., it does not form a strong, extended bar by our criterion, even after 4 Gyr. In model r1c14ldmsf1, which features greater instability, a bar still forms but appears substantially weaker and shorter. As conjectured in Section 3.1, this suggests that the threshold of maximum DM softening length for bar formation varies depending on the disk stability. However, even when bars form despite an excessive DM softening length, their growth may not be well promoted by the absence of the central angular momentum exchange.

To examine the effects of large DM softening alone ($\epsilon_{\text{DM}} = 0.96$ kpc) without mixing the DM resolution effects, we evolve model r1c16sf1, which has the same resolution with model r1c16 ($N_{\text{DM}} = 1.14 \times 10^7$ and $m_{\text{DM}}/m_{\star} = 10$) but differs only in the DM softening length, increased from $\epsilon_{\text{DM}} = 0.03$ kpc to 0.96 kpc. In Figure 3, we visualize the time evolution of the Fourier modes

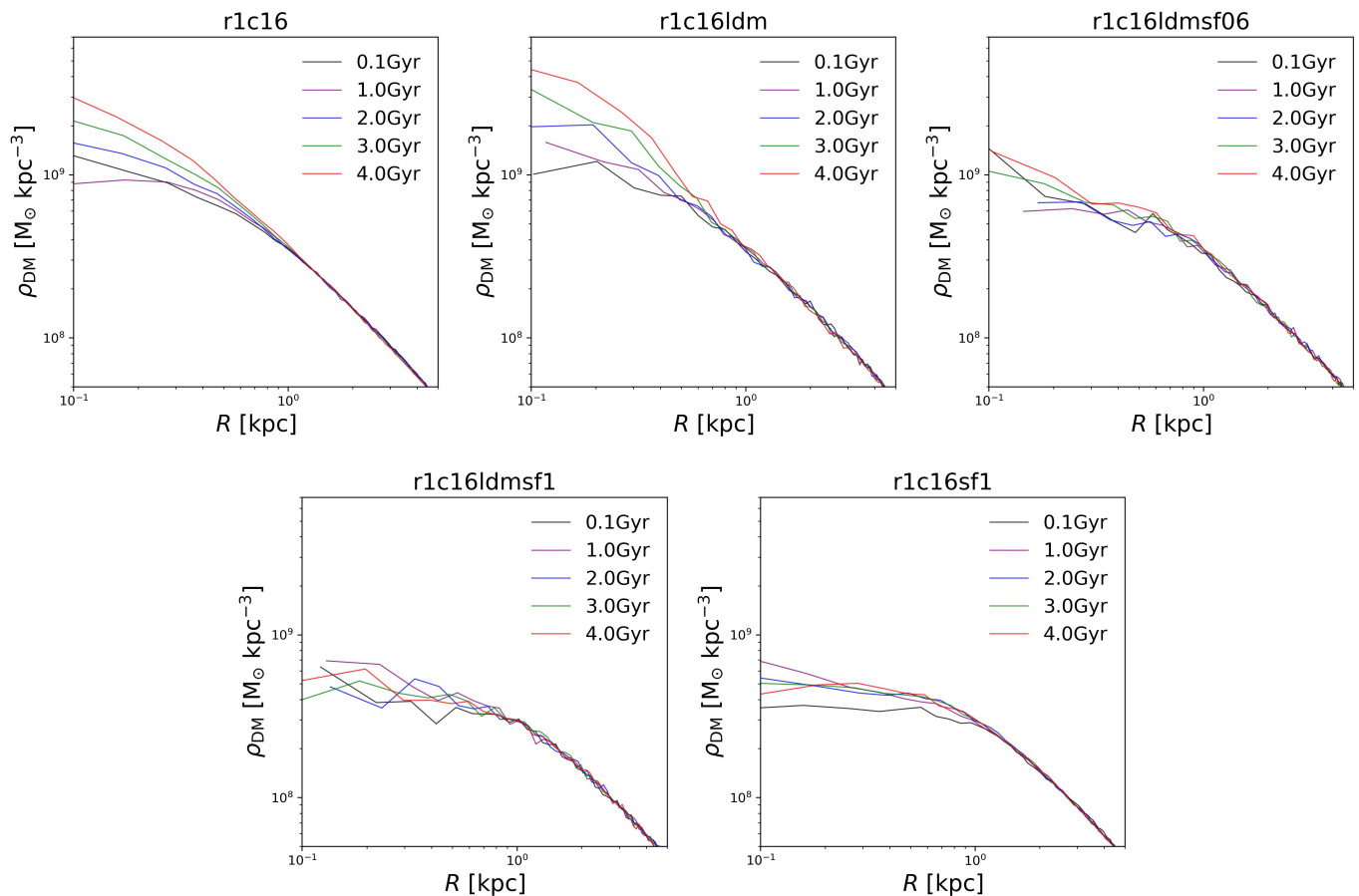


Fig. 6: Radial density profiles of the DM halo in the ‘c16’ models from 0.1 Gyr to 4 Gyr, shown between 0.1 kpc and 5 kpc. Both axes are logarithmic. Profiles at different times are color-coded and labeled accordingly.

($m = 1$ to 6) and F_{sum} , where $F_{\text{sum}}(R) = \sqrt{\sum_{m=1}^6 [F_m(R)]^2}$. Note that similar figures in Paper I use a color bar scale ranging from 1% to 15% to highlight spirals in the corresponding modes, whereas here we adopt a scale from 1% to 40% to emphasize the bar mode.

As introduced in Paper I, multi-mode spirals emerge sequentially from higher to lower modes, accompanied by a decaying epicenter (e.g., $m = 5$ and 6 appear in the outer region of model r2c16, followed by lower modes in the inner region; Fig. 6 in Paper I) This mode cascade proceeds without significant angular momentum loss to the halo until reaching $m = 3$, at which point the spiral phase transitions to the bar phase through central mode amplification and subsequent dynamical friction from the DM halo. Capturing this natural mode evolution requires sufficient resolution and an appropriate mass ratio.

Model r1c16sf1 also displays such mode cascading during multi-mode spiral formation: the $m = 6$ spiral appears first around 6 kpc, followed by lower modes. The $m = 3$ mode emerges toward the central region where central angular momentum exchange plays a crucial role in the subsequent bar formation. However, owing to the unresolved star-DM interaction within $R \approx 1$ kpc, the amplitude of the $m = 2$ mode in the central region remains faint throughout the 4 Gyr evolution. Consequently, the model fails to develop a strong bar despite sufficient DM resolution.

Comparing the F_2 amplitude in model r1c16sf1 with that of model r1c16ldmsf1 in Figure 2, the amplitude appears even more

suppressed in r1c16sf1. We conjecture that the massive DM particles in r1c16ldmsf1 ($m_{\text{DM}}/m_{\star} = 100$) introduce numerical perturbations that contribute to the initial F_2 amplification. Still, neither model develop a bar-like structure with $F_2 > 0.3$ by 4 Gyr, likely due to the unresolved angular momentum exchange within $R \approx 1$ kpc when $\epsilon_{\text{DM}} = 0.96$ kpc.

In Figure 4, we present the maximum value of F_2 within 20 kpc as a function of time. To improve visibility, we apply smoothing using a moving average over 9 points. The raw data without smoothing are shown in Figure A.1, which exhibit a wide range of oscillations due to bar-spiral periodic overlap (Hilmi et al. 2020; Marques et al. 2025). In models r1c16ldmsf1 and r1c16sf1, which do not develop stable, extended bars, these oscillations reflect recurrent episodes of transient inner $m = 2$ distortions that do not settle into a coherent bar (Fig. A.1). Their stellar disks remain unstable due to the combination of stability and numerical perturbations, but the lack of angular momentum transfer prevents the phase transition to the bar formation, thereby sustaining these fluctuations until the end of their evolution.

Models r1c16 and r1c16ldm with $\epsilon_{\text{DM}} = 0.03$ kpc form the strongest bars among the ‘c16’ models, reaching $F_{2,\text{max}} \approx 0.5$, whereas models with larger softening attain lower peak values (Fig. 4). Both ‘sf1’ models fail to grow beyond $F_2 = 0.3$, although r1c16ldmsf1 reaches a slightly higher value owing to enhanced instability from perturbations driven by massive DM particles. Model r1c14ldmsf1 reaches $F_2 \approx 0.3$ but does not

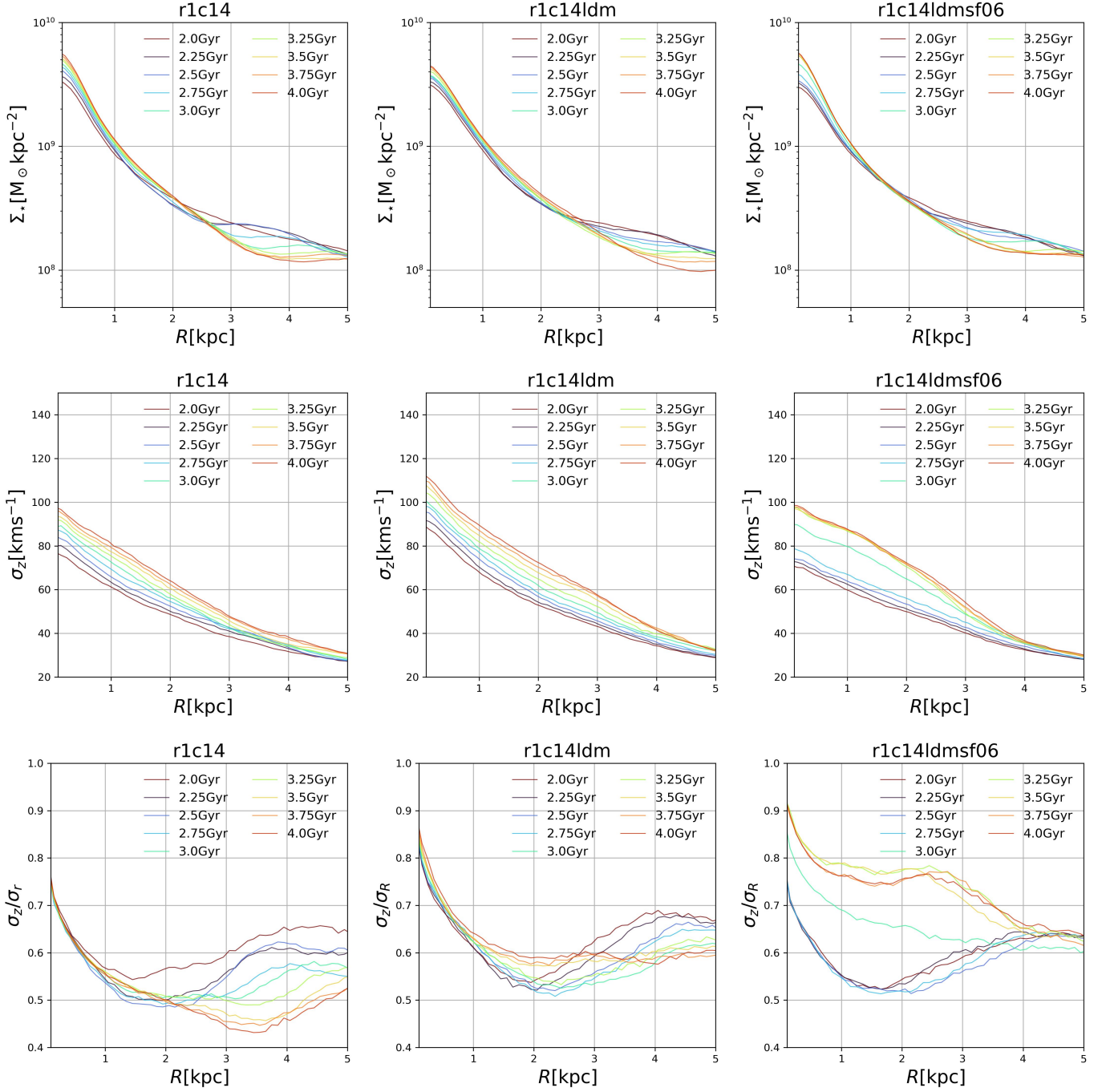


Fig. 7: The radial profiles of stellar disk properties within 5 kpc, from 2 Gyr to 4 Gyr with a timestep of 0.25 Gyr. The left, middle, and right columns correspond to models r1c14, r1c14ldm, and r1c14ldmsf06, respectively, all of which form a bar. The top row shows the density profiles for each model. The middle row shows the vertical velocity dispersion of the disk. The bottom row shows the ratio between the vertical and radial velocity dispersions.

grow further due to the absence of central angular momentum exchange.

The ‘c14’ models, except for r1c14ldmsf1, follow similar bar evolution paths until they diverge due to vertical buckling instability. Note that increasing the DM resolution to $m_{\text{DM}}/m_{\star} = 1$ in model r1c14hdm does not substantially alter the evolution of bar strength relative to model r1c14 with $m_{\text{DM}}/m_{\star} = 10$ (Appendix B). Although more unstable disks, such as those in the ‘c14’ models, are less sensitive to resolution effects regarding the bar formation epoch, variations in softening length notice-

ably affect bar strength during the post-buckling phase. In Figure 4, the bar strength in model r1c14ldmsf06 decreases by 0.2 from $F_2 \approx 0.56$, whereas r1c14 continues to grow and r1c14ldm undergoes gradual bar weakening. In model r1c14ldmsf03 (Appendix B), the buckling instability rapidly decreases the bar strength by 0.08 from $F_2 \approx 0.48$ around 2.2 Gyr (Fig. B.1). This indicates an inverse correlation between the DM softening length and the magnitude of buckling-induced weakening in F_2 .

To quantify the angular momentum transferred from stars to DM halos, we measure the total disk angular momentum

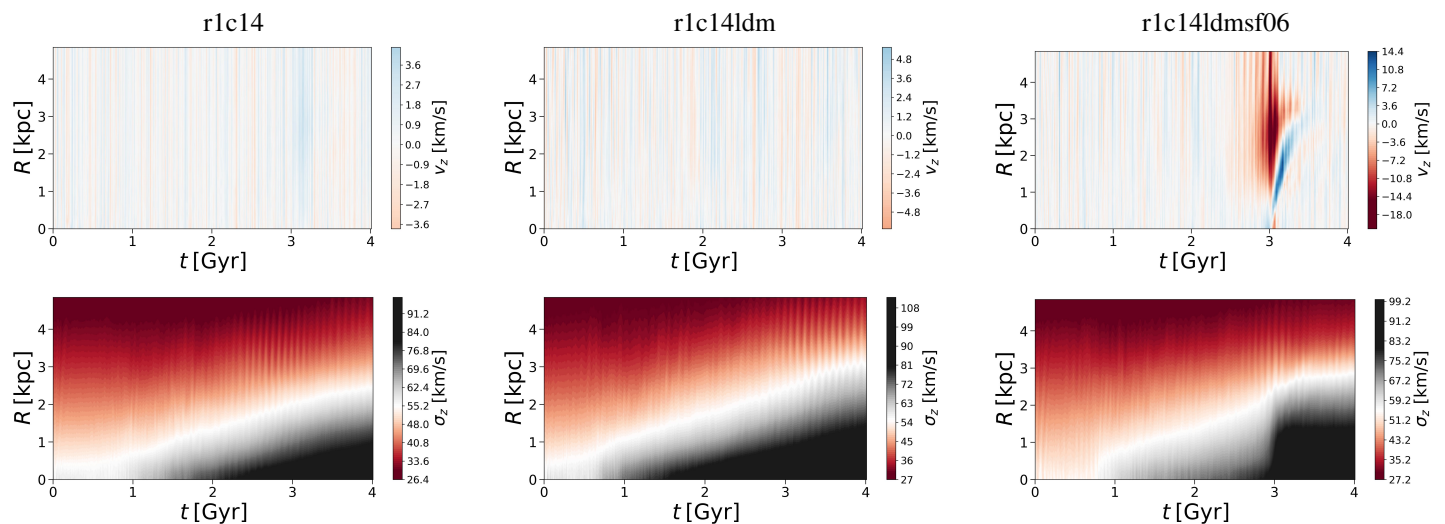


Fig. 8: Time evolution of the radial distribution of v_z (top panels) and σ_z (bottom panels) in the stellar disks over 4 Gyr. The left, middle, and right columns correspond to models r1c14, r1c14ldm, and r1c14ldmsf06, respectively. For v_z , the color bar ranges from -15 to 15 km s $^{-1}$. Sudden fluctuations in the v_z map indicate the buckling instability. For σ_z , the color bar ranges from 30 to 80 km s $^{-1}$, and the black regions indicate vertical heating of the stellar disk.

L_z normalized by its initial value $L_{z,0}$ in Figure 5. The exchange of angular momentum between stars and DM particles serves as the primary mechanism driving bar formation (Athanasoula 2002, 2003; Kwak et al. 2017, 2019). The extent of this angular momentum transfer correlates with the bar’s strength and length. As the stellar bar transfers angular momentum to the DM halo, it decelerates and strengthens, which in turn elevates the radial velocity dispersion of stars and eventually triggers vertical buckling instability (Raha et al. 1991; Combes et al. 1990; Martinez-Valpuesta & Shlosman 2004; Martinez-Valpuesta et al. 2006; Debattista et al. 2006; Kwak et al. 2017, 2019; Łokas 2019a,b, 2025a). In the ‘c16’ models, r1c16ldm, which forms the strongest bar, exhibits the greatest angular momentum loss. This may arise because massive DM particles are more effective at facilitating angular momentum exchange during the early phases when the bar is relatively weak. Compared to r1c16, model r1c16ldmsf06 forms a less strong bar and thus loses less angular momentum, reflecting an inverse correlation between DM softening length and bar strength, as illustrated in Figures 2 and 4. In the ‘c14’ models, which form strong bars, the total stellar angular momentum loss reflects the combined effects of resolution and DM softening length in an inverse manner: higher resolution and smaller softening boost the angular momentum exchange more effectively. The difference is small between models r1c14 and r1c14ldm, attributable to gradual bar weakening in r1c14ldm around 3.5 Gyr, whereas the bar in r1c14 continuously grows longer ($R > 4$ kpc where $F_2 > 0.3$ in Fig. 2).

The DM softening length induces more pronounced changes in bar formation and buckling instability than resolution effects alone. To investigate this, we measure the spherical density profile of the DM halo, ρ_{DM} , from 0.1 kpc to 5 kpc on a log-log scale in Figure 6. We present only the ‘c16’ models, as the density profiles of the ‘c14’ models are similar for equivalent resolution and softening lengths. In the ‘sf1’ models ($\epsilon_{\text{DM}} = 0.96$ kpc), the central density profiles flatten in the inner 1 kpc regardless of DM halo resolution, remaining around $\rho_{\text{DM}} \approx 5 \times 10^8$ M $_{\odot}$ kpc $^{-3}$ throughout the evolution. This flattening is a well-known numerical artifact in cosmological simulations, where Plummer

or spline softening mitigates two-body relaxation and noise but under-resolves gravitational forces on scales below the softening length, yielding a spurious core instead of the expected cusp (Fukushige & Makino 2001; Power et al. 2003; Diemand et al. 2005). Therefore, the softened potential inhibits tight particle clustering in the center. The effect persists independent of particle number once convergence is reached and scales directly with the softening length. In our initial conditions, the central cusp hosts most DM particles, but unresolved interactions within the softening length prevent them from staying bound at the very center, thus eroding the cusp rapidly. In addition to the bar weakening effects, larger softening lengths exacerbate this central flattening. By contrast, models r1c16 and r1c16ldm sustain $\rho_{\text{DM}} > 10^9$ M $_{\odot}$ kpc $^{-3}$, with gradual increases over time. In general, a reduction in the central mass concentration of the spheroidal component tends to destabilize the disk and promote bar formation (Kwak et al. 2017; Kataria & Das 2018; Jang & Kim 2023). However, our results indicate that central mass concentration alone is insufficient to produce a strong bar unless accompanied by efficient angular momentum transfer (Athanasoula 2002, 2003), particularly in the central region where a nascent bar begins to grow.

3.3. Resolution and Softening on Buckling Instability

The buckling instability in galactic bars is a vertical bending mode that thickens the bar out of the disk plane, often leading to the formation of boxy or peanut-shaped bulges, as the bar’s self-gravity amplifies asymmetries in the velocity distribution (Combes et al. 1990; Raha et al. 1991; Kwak et al. 2017, 2019; Łokas 2019a,b, 2025a). It is often associated with anisotropy in the stellar velocity dispersions, where excessive radial heating from the bar’s growth creates an imbalance and triggers out-of-plane oscillations when the vertical support becomes insufficient (Merritt & Sellwood 1994). A live halo can promote angular momentum exchange and thereby enable stronger bar growth, which can lead to buckling instability (Berentzen et al. 2006). A common criterion for its onset is when the ratio of vertical to radial velocity dispersion, σ_z/σ_R , drops below 0.5–0.6, although

this threshold can vary with factors such as the bar’s properties, the presence of a gaseous component, and the halo’s dynamical influence (Debattista et al. 2006; Kwak et al. 2017, 2019; Seo et al. 2019; Jang & Kim 2024; Jang et al. 2025). Moreover, the peanut/X-shape can track the radius of the bar’s 2:1 vertical resonance and migrate outward as the bar slows and the disc thickens (Quillen et al. 2014). Accordingly, the presence of a peanut/X-shape alone is not uniquely diagnostic of a distinct buckling episode; we therefore rely primarily on kinematic diagnostics, such as σ_z/σ_R .

In Figure 7, we examine the radial profiles of surface density, vertical velocity dispersion σ_z , and the ratio σ_z/σ_R for models r1c14, r1c14ldm, and r1c14ldmsf06 to visualize the impacts of DM resolution and softening on buckling instability. These models are chosen as they follow comparable bar evolutionary paths until divergence arises from vertical buckling instability. To capture the transitions in these properties from the pre- to post-buckling phases, we compute them starting at 2 Gyr and extending to 4 Gyr with a timestep of 0.25 Gyr. Overall, as evolution proceeds, the surface density in these bar-forming models increasingly contracts and becomes centrally concentrated (e.g., see Fig. 6 in Kwak et al. 2017).

The vertical velocity dispersion increases gradually in most models, except for r1c14ldmsf06, which undergoes a strong buckling instability that vertically perturbs and thickens the stellar components (Fig. 7). In model r1c14, the central σ_z ranges from approximately 80 to 100 km s^{-1} , whereas in r1c14ldm it is about 10% higher (90 to 110 km s^{-1}), attributable to spurious numerical heating induced by massive DM particles (Ludlow et al. 2021). In contrast, model r1c14ldmsf06 exhibits a sudden increase in σ_z at 2.75 Gyr, when it reaches slightly below 80 km s^{-1} . This coincides with the epoch of abrupt bar strength decline (Fig. 4). Although models r1c14ldm and r1c14ldmsf06 share the same DM resolution, the numerical disk heating from massive DM particles is far less effective in r1c14ldmsf06 due to its larger softening length ($\epsilon_{\text{DM}} = 0.60$ kpc), resulting in central σ_z values more than 20% lower relative to r1c14ldm ($\epsilon_{\text{DM}} = 0.03$ kpc). The vertical velocity dispersion σ_z acts as a stabilizing factor against the onset and recurrence of buckling instability. For instance, Kwak et al. (2017) showed that the initial buckling event occurs in the inner bar, elevating local σ_z and thereby shifting subsequent recurrences to outer regions less affected by the prior vertical heating.

The ratio σ_z/σ_R differs markedly among the three models in the bottom panels of Figure 7. In the models with lower DM halo resolution (model r1c14ldm and r1c14ldmsf06), this ratio does not drop below ~ 0.5 , whereas in r1c14—which sustains continuous growth of a well-elongated bar extending beyond 4 kpc without weakening—the ratio falls below 0.5 for $R > 3$ kpc by 4 Gyr. Model r1c14ldm, which experiences gradual vertical instability from 3.25 to 4 Gyr (Fig. 4), shows σ_z/σ_R rise to ≈ 0.6 after approaching ≈ 0.5 . The underlying mechanism driving this gradual bar weakening in the outer region due to DM resolution differences remains unclear and requires further investigation in the future in light of the radial distribution of the vertical instability threshold. As noted in Kwak et al. (2017), initially hotter discs undergo vertical instability earlier in the outer regions (see their models DP3 and DP4 in Figure 14). We therefore conjecture that the elevated disk heating (σ_R and σ_z) in model r1c14ldm, induced by spurious heating from massive DM particles prior to bar formation, likely triggers the vertical instability once the bar extends to outer regions at $R \approx 4$ kpc. Apart from the resolution effects ($m_{\text{DM}}/m_\star = 100$), model r1c14ldmsf06

displays a pronounced increase in σ_z/σ_R owing to its strong buckling instability.

To trace the occurrence of buckling instability, we present radial distribution maps of v_z and σ_z as functions of time in Figure 8. The color bars are fixed, ranging from -15 to 15 km s^{-1} for v_z and from 30 to 80 km s^{-1} for σ_z , ensuring that identical colors represent equivalent values across models. Models r1c14 and r1c14ldm exhibit no visible changes in v_z , whereas r1c14ldmsf06 displays pronounced fluctuations around 3 Gyr, coinciding with a substantial decline in bar strength (Fig. 4). The duration of elevated v_z is approximately 0.5 Gyr, aligning with the period during which the bar strength F_2 decreases from 0.56 to 0.36 (Fig. 4).

Given that Figure 7 indicates lower pre-buckling σ_z in r1c14ldmsf06 compared to r1c14ldm, we also visualize the σ_z distribution in the bottom panels of Figure 8. This clearly reveals that the two models with $\epsilon_{\text{DM}} = 0.03$ kpc undergo gradual vertical heating in the central region during bar formation and growth. Again, model r1c14ldm ($m_{\text{DM}}/m_\star = 1$) undergoes nearly the same bar formation without buckling instability, implying that this is not a mass ratio effect (Fig. B.1). In contrast, model r1c14ldmsf06 ($\epsilon_{\text{DM}} = 0.60$ kpc) exhibits no such gradual vertical heating in the central region during the same phase of bar formation. Notably, all three models maintain nearly equivalent bar strengths F_2 until shortly before the buckling instability before 3 Gyr. Despite these comparable bar strengths, the failure to resolve central σ_z —a key stabilizing factor against buckling—leads to a greater imbalance in σ_z/σ_R , thereby triggering a stronger buckling instability in model r1c14ldmsf06 (e.g., Debattista et al. 2006; Kwak et al. 2017).

4. Discussion and Conclusion

Using N-body simulations, we investigate the effects of resolution and gravitational softening in the DM halo on bar formation and buckling instability. In our dissipationless, isolated disk-halo systems, we fix the stellar disk parameters and vary the resolution, softening length, and concentration parameter of the DM halo, as changes in the DM fraction alter the stability of the disks. Across two different levels of stability, we examine the relative effects of m_{DM}/m_\star and ϵ_{DM} on the bar formation epoch, the evolutionary path of bar properties, and bar weakening via buckling instability.

4.1. DM Resolution on Bar Formation

The formation of non-axisymmetric structures, such as bars, exhibits a sensitivity to numerical noise that is modulated by the intrinsic stability of the disk: more unstable disks show reduced variability in the formation epoch due to shot noise (Paper I). Enhancing the resolution of both the stellar disk and the DM halo by a factor of 10 relative to the ‘r1’ models results in a delay in bar formation (0.5 Gyr for the ‘c14’ models and 1.9 Gyr for the ‘c16’ models). This delay stems from a substantial reduction in Poisson noise within the entire system, which suppresses the generation of noise-induced perturbations and spirals. These spirals otherwise cascade toward the center, augmenting bar formation beyond the disk’s intrinsic instability.

Similarly, increasing solely the DM halo resolution by a factor of 10 induces a delay (0.1 Gyr in ‘c14’ and 0.9 Gyr in ‘c16’ models), albeit for a distinct reason: the angular momentum transfer imparted by more massive DM particles is mitigated when $m_{\text{DM}}/m_\star = 1$ during the transitional phase from spirals to

bars. Conversely, decreasing the DM halo resolution by a factor of 10 also delays bar formation, driven by yet another mechanism: the passage of massive DM particles ($m_{\text{DM}}/m_{\star} = 100$) through the disk plane sporadically and continuously exerts gravitational shocks all over the disk, thereby heating the disk globally and enhancing its stability. For instance, the NewHorizon simulation (Dubois et al. 2021) reported the “missing bar” problem (Reddish et al. 2022) while adopting $m_{\text{DM}} = 1.2 \times 10^6$ and $m_{\text{DM}}/m_{\star} \approx 92$. Ludlow et al. (2021) has already pointed out that such low DM resolution ($N_{\text{DM}} \lesssim 10^6$ and $m_{\text{DM}} \gtrsim 10^6 M_{\odot}$) artificially elevates the vertical velocity dispersion due to collisional heating on stellar disks. In addition to that, our findings suggest that the global increase in F_{sum} induced by high m_{DM}/m_{\star} introduces another numerical artifact stabilizing the stellar disks against the bar instability. The impacts of stellar disk and DM halo resolution on the bar formation epoch are intricate with various underlying mechanisms. This complexity demands meticulous attention when configuring galaxy models, particularly those residing in the *stable* regime of the stability spectrum.

The stable regime, as discussed in Paper I and the present work, covers a broad range of disk stabilities, with the ‘c16’ model positioned approximately in the middle of this spectrum. Indeed, model r1c16 develops a bar at 1.67 Gyr, defined by $F_2 > 0.3$, and achieves a peak strength of $F_2 \approx 0.5$ shortly after 2 Gyr. This timescale is relatively brief for bar formation compared to the Hubble time.

For comparison, Jang et al. (2025) examined bar formation conditions in galaxies using $N_{\star} = 10^6$ and $N_{\text{DM}} = 2 \times 10^7$, with particle masses of $m_{\star} \approx 5 \times 10^4 M_{\odot}$ and $m_{\text{DM}}/m_{\star} \approx 2$ in their Milky Way-mass models. Regarding the impact of disk resolution on spiral formation and associated disk heating, Fujii et al. (2011) analyzed numerical effects on spiral structures and their lifetimes (employing $N_{\star} = 3 \times 10^5$ to 3×10^7) and determined that a sufficient number of disk particles (e.g., $N_{\star} \gtrsim 3 \times 10^6$) is essential to sustain spirals without external cooling. Models with fewer star particles generate spirals predominantly through numerical noise, resulting in earlier development and over-amplification (see their Fig. 7). These noise-induced spirals transport perturbations more rapidly and prematurely to the central region, thereby initiating DM-star dynamical friction and accelerating bar formation. This process accounts for the observed 1.9 Gyr delay in bar formation when increasing resolution from $N_{\star} = 5 \times 10^6$ to 5×10^7 with $m_{\text{DM}}/m_{\star} = 10$ in model r1c16 and r2c16 in Paper I. Furthermore, bars in the Jang et al. (2025) models form between approximately 3.5 and 6.7 Gyr, indicating that their disk-halo models are more stable than our r1c16 model and thus more susceptible to numerical noise affecting the timing of bar formation. Such resolution-dependent delays in bar formation have been also reported by Dubinski et al. (2009). Hence, we conjecture that re-simulating these stable models with $N_{\star} = 5 \times 10^7$ stellar particles and $m_{\text{DM}}/m_{\star} < 10$, which reduce initial noise levels $F_{\text{sum}} \approx 0\%$ (Paper I), could prevent bar formation within the Hubble time in certain cases.

In practice, employing such a large number of particles to generate nearly noise-free initial conditions is challenging. In low DM resolution cases with $m_{\text{DM}}/m_{\star} = 100$, surprisingly, the bar formation timing exhibits no substantial difference, although the evolutionary paths diverge later owing to accumulated numerical effects from massive DM particles. For instance, the bar strength peaks lower and experiences bar weakening in model r1c14ldm compared to the high DM resolution models. Note that our models are idealized disk-halo setup, and $m_{\text{DM}}/m_{\star} = 100$ would result more significant effects during the hierarchical formation (Ludlow et al. 2019, 2023). Fortunately, the evolution-

ary path of model r1c14hdm ($m_{\text{DM}}/m_{\star} = 1$), which employs 10 times more DM particles, is comparable to that of model r1c14, as evidenced by their similar evolution of bar strength and angular momentum transfer (Fig. B.1). We therefore suggest that a resolution comparable to that of model r1c14 ($m_{\text{DM}}/m_{\star} = 10$, $m_{\star} = 10^4 M_{\odot}$, and $N_{\star} = 5 \times 10^6$) may not significantly alter the outcomes when simulating such *unstable* galaxies driven by strong self-instabilities or tidal forcing (Łokas et al. 2014, 2016; Łokas 2019b; Kwak et al. 2019; Bekki 2023). For relatively stable models in which bars form gradually after 2 Gyr, the influence of resolution on bar properties, particularly the formation epoch, must be carefully considered.

4.2. Softening Effects on Bar Strength and Buckling Instability

The DM softening effect is more pronounced than that of DM resolution on bar formation. Note that Iannuzzi & Athanassoula (2013) found no significant differences between fixed and adaptive softening lengths, but their chosen softening length was much smaller than ours (e.g., $\epsilon = 0.05$ kpc in the fixed model). While the inner 1 kpc region may appear insignificant relative to the scale radius and virial radius of the DM halo, the central angular momentum exchange plays a crucial role, particularly during the early phases of bar formation. In these stages, the seed bar remains small and grows via dynamical friction between DM particles and stars. Consequently, insufficient angular momentum transfer arising from an excessively large DM softening length can substantially delay or entirely prevent bar formation.

This may provide an additional factor suppressing bar formation and growth in the NewHorizon simulation (Dubois et al. 2021; Reddish et al. 2022), which uses $\epsilon_{\text{DM}} = 0.32$ kpc at $z = 2-0.25$ and $\epsilon_{\text{DM}} = 0.50$ kpc at $z = 0.25-0$. Reddish et al. (2022) presented only one visually confirmed bar, with a length of $R(F_2 > 0.3) \approx 0.6$ kpc, in their Figures 1 and 8. This small bar persists from $z = 1.3$ to $z = 0.7$, and the host galaxy is the most massive disk. Note that the ‘sf1’ models ($\epsilon_{\text{DM}} = 0.94$ kpc) develop only an oval or short bar that fails to grow beyond ~ 3 kpc (roughly $3 \times \epsilon_{\text{DM}}$), which implies that the $\epsilon_{\text{DM}} = 0.32$ kpc adopted in Reddish et al. (2022) is relatively large compared to their bar length. In general, low DM mass resolution results in larger and hotter stellar disks with colder halos (Ludlow et al. 2023) and produces fewer halos owing to the inability to properly resolve dwarf-sized DM halos (Revaz & Jablonka 2018; Ludlow et al. 2019). This consequently omits a fraction of mergers during hierarchical formation, potentially leading to more DM-dominated galaxies among lower-mass systems, which is also observed in Reddish et al. (2022). Despite these potentially stabilizing effects associated with their mass resolution, their most massive disk could be gravitationally more unstable and become more prone to bar formation, presumably triggered by tidal forcing. This may enable the emergence of a nascent bar, but the large ϵ_{DM} adopted impedes its subsequent growth via angular momentum transfer, akin to the case in our model r1c14ldmsf1 (Fig. 1) and the case in Kaufmann et al. (2007).

Sufficient resolution and an appropriate ϵ_{DM} are important, but cannot be the only explanation for the missing bar problem. For example, the Auriga simulation (Grand et al. 2017) and the Hestia simulation (Libeskind et al. 2020) adopt the same model, yet Hestia still suffers from the missing bar problem despite its higher resolution, presumably owing to different initial conditions. In the fully cosmological context, many inter-related factors come into play. Different merger histories can

alter the masses of classical bulges: more massive bulges increase the central mass concentration and suppress bar instability (Athanasoula et al. 2005; Kwak et al. 2017; Kataria & Das 2018; Saha & Elmegreen 2018; Jang & Kim 2023). In addition, high gas fractions tend to form weaker and shorter stellar bars by damping disk instabilities and angular momentum transfer (Athanasoula et al. 2013; Seo et al. 2019; Łokas 2020; Beane et al. 2023). In highly turbulent, gas-rich environments, elevated gas content can even dissolve bars through enhanced dissipation, converting them into central bulges as star formation-driven kinematic heating disrupts non-axisymmetric structures (Bland-Hawthorn et al. 2024). Hence, these effects on the bar formation merit further investigation in future studies.

Overall, the cumulative effects of ϵ_{DM} over time from the missing central angular momentum exchange reduce the final bar strength, leading models with larger softening parameters to exhibit weaker bars and lower peak bar strengths throughout their evolution. Considering the nearly identical evolutionary paths of bar strength in models r1c14 and r1c14hdm with $\epsilon_{\text{DM}} = 0.03$ kpc, adopting $\epsilon_{\text{DM}} \geq 0.3$ kpc has a much greater impact than adopting $m_{\text{DM}}/m_{\star} \geq 10$ (Fig. B.1).

Additionally, larger DM softening lengths (e.g., $\epsilon_{\text{DM}} \geq 0.30$ kpc) may over-produce the buckling instability, which also eventually weakens the bar strength. A bar rotates and slows down by transferring its angular momentum to the DM halo, thereby growing stronger and increasing the radial velocity dispersion σ_R (Athanasoula 2003; Kwak et al. 2017). In this context, the location of the bar's 2:1 vertical resonance (and thus the peanut/X signature) can migrate outward as the bar slows and the disk thickens (Quillen et al. 2014). Regardless of DM resolution, in bar-forming models with $\epsilon_{\text{DM}} = 0.03$ kpc, the vertical velocity dispersion σ_z gradually increases, starting from the very center. A thicker disk or higher velocity dispersion serves as a stabilizing factor against the onset of buckling instability. In studies examining the effects of disk thickness on the evolution of barred galaxies, Klypin et al. (2009) and Kwak et al. (2017) found that thinner disks form shorter bars and undergo buckling instability earlier than their thicker counterparts. However, large softening lengths prevent the gradual vertical heating in the central region during the bar formation, resulting in a numerically induced larger imbalance in σ_z/σ_R that triggers a stronger buckling instability. We find that the decrease in bar strength due to buckling instability intensifies as ϵ_{DM} increases from 0.03 to 0.30 to 0.60 kpc (Fig. B.1). Notably, softening lengths in this range ($\epsilon_{\text{DM}} = 0.30 - 0.60$ kpc) are commonly adopted in cosmological and zoom-in simulations, including EAGLE (Schaye et al. 2015), ILLUSTRIS TNG (Pillepich et al. 2018b,a, 2019), AURIGA (level 4) (Grand et al. 2017), and NEWHORIZON (Dubois et al. 2021). Similarly, some studies also adopted $\epsilon_{\text{DM}} = 0.7$ kpc in their idealized disk-halo systems (Łokas et al. 2016; Semczuk et al. 2017; Łokas 2018, 2019b). We conjecture that the central vertical velocity dispersion $\sigma_z(R < \epsilon_{\text{DM}})$ may be systematically underestimated with $\epsilon_{\text{DM}} \geq 0.3$ kpc, unless a bar undergoes numerically enhanced buckling, which then eventually lowers the peak bar strength F_2 .

In conclusion, from a practical standpoint, we recommend adopting $m_{\text{DM}}/m_{\star} \leq 10$, $m_{\star} \leq 10^4 M_{\odot}$, and $N_{\star} \geq 5 \times 10^6$ when investigating the formation and evolution of non-axisymmetric structures in Milky Way-mass galaxies. Determining the resolution at which the outcomes of bar instability converge would be interesting, but achieving an effectively noise-free system by indefinitely increasing the number of particles is impractical given

current computational resources. In real galaxies, natural noise levels of $F_{\text{sum}} \geq 1\%$ may arise over time from processes such as stellar feedback (Marinacci et al. 2019), the presence of numerous globular clusters (D'Onghia et al. 2013), and tidal forcing by satellites (Łokas et al. 2014, 2016; Kwak et al. 2019). In our N-body models, $F_{\text{sum}} \approx 1\%$ leads to significant divergence in the timing of bar formation. We anticipate that such noise effects on bar timing would be less pronounced in gaseous galaxy models with realistic stellar feedback, although this requires further investigation to confirm. Regarding gravitational softening, our models with $\epsilon_{\text{DM}} \geq 0.30$ kpc exhibit considerable divergence, producing multiple bar weakening or strong buckling even in the unstable regime. This amplifies the radial-vertical velocity dispersion anisotropy and triggers vertical instabilities. In the future, smaller ($\epsilon_{\text{DM}} < 0.30$ kpc) or adaptive DM softening lengths (Iannuzzi & Athanasoula 2013) in the central region, potentially scaled by the galaxy's effective radius depending on its mass and size, may be needed to properly resolve the central DM-star interactions and to prevent numerical vertical instabilities.

Acknowledgements. IM acknowledges support by the Deutsche Forschungsgemeinschaft under the grant MI 2009/2-1.

References

- Ansar, S., Pearson, S., Sanderson, R. E., et al. 2025, *ApJ*, 978, 37
 Athanasoula, E. 2002, *ApJ*, 569, L83
 Athanasoula, E. 2003, *MNRAS*, 341, 1179
 Athanasoula, E. 2014, *MNRAS*, 438, L81
 Athanasoula, E., Lambert, J. C., & Dehnen, W. 2005, *MNRAS*, 363, 496
 Athanasoula, E., Machado, R. E. G., & Rodionov, S. A. 2013, *MNRAS*, 429, 1949
 Athanasoula, E. & Sellwood, J. A. 1986, *MNRAS*, 221, 213
 Beane, A., Hernquist, L., D'Onghia, E., et al. 2023, *ApJ*, 953, 173
 Bekki, K. 2023, *MNRAS*, 523, 5823
 Berentzen, I., Shlosman, I., & Jogee, S. 2006, *ApJ*, 637, 582
 Bland-Hawthorn, J., Tepper-Garcia, T., Agertz, O., & Federrath, C. 2024, *ApJ*, 968, 86
 Bose, S., Eisenstein, D. J., Hernquist, L., et al. 2019, *MNRAS*, 490, 5693
 Combes, F., Debbasch, F., Friedli, D., & Pfenniger, D. 1990, *A&A*, 233, 82
 Debattista, V. P., Mayer, L., Carollo, C. M., et al. 2006, *ApJ*, 645, 209
 Diemand, J., Zemp, M., Moore, B., Stadel, J., & Carollo, C. M. 2005, *MNRAS*, 364, 665
 D'Onghia, E., Vogelsberger, M., & Hernquist, L. 2013, *ApJ*, 766, 34
 Dubinski, J., Berentzen, I., & Shlosman, I. 2009, *ApJ*, 697, 293
 Dubois, Y., Beckmann, R., Bournaud, F., et al. 2021, *A&A*, 651, A109
 Efstathiou, G., Lake, G., & Negroponte, J. 1982, *MNRAS*, 199, 1069
 Fall, S. M. & Efstathiou, G. 1980, *MNRAS*, 193, 189
 Fujii, M. S., Baba, J., Saitoh, T. R., et al. 2011, *ApJ*, 730, 109
 Fukushige, T. & Makino, J. 2001, *ApJ*, 557, 533
 Grand, R. J. J., Gómez, F. A., Marinacci, F., et al. 2017, *MNRAS*, 467, 179
 Hernquist, L. 1990, *ApJ*, 356, 359
 Hernquist, L. & Barnes, J. E. 1990, *ApJ*, 349, 562
 Hilmi, T., Minchev, I., Buck, T., et al. 2020, *MNRAS*, 497, 933
 Iannuzzi, F. & Athanasoula, E. 2013, *MNRAS*, 436, 1161
 Jang, D. & Kim, W.-T. 2023, *ApJ*, 942, 106
 Jang, D. & Kim, W.-T. 2024, *ApJ*, 971, 67
 Jang, D., Kim, W.-T., & Lee, Y. H. 2025, *ApJ*, 993, 236
 Kataria, S. K. & Das, M. 2018, *MNRAS*, 475, 1653
 Kaufmann, T., Mayer, L., Wadsley, J., Stadel, J., & Moore, B. 2007, *MNRAS*, 375, 53
 Klypin, A., Valenzuela, O., Colín, P., & Quinn, T. 2009, *MNRAS*, 398, 1027
 Kwak, S., Kim, W.-T., Rey, S.-C., & Kim, S. 2017, *ApJ*, 839, 24
 Kwak, S., Kim, W.-T., Rey, S.-C., & Quinn, T. R. 2019, *ApJ*, 887, 139
 Kwak, S., Minchev, I., Pfrommer, C., Steinmetz, M., & Yi, S. K. 2025, arXiv e-prints, arXiv:2511.21805
 Libeskind, N. I., Carlesi, E., Grand, R. J. J., et al. 2020, *MNRAS*, 498, 2968
 Łokas, E. L. 2018, *ApJ*, 857, 6
 Łokas, E. L. 2019a, *A&A*, 629, A52
 Łokas, E. L. 2019b, *A&A*, 624, A37
 Łokas, E. L. 2020, *A&A*, 634, A122
 Łokas, E. L. 2025a, *A&A*, 699, A234

- Lokas, E. L. 2025b, *A&A*, 702, A7
- Lokas, E. L., Athanassoula, E., Debattista, V. P., et al. 2014, *MNRAS*, 445, 1339
- Lokas, E. L., Ebrova, I., del Pino, A., et al. 2016, *ApJ*, 826, 227
- Ludlow, A. D., Fall, S. M., Schaye, J., & Obreschkow, D. 2021, *MNRAS*, 508, 5114
- Ludlow, A. D., Fall, S. M., Wilkinson, M. J., Schaye, J., & Obreschkow, D. 2023, *MNRAS*, 525, 5614
- Ludlow, A. D., Schaye, J., Schaller, M., & Richings, J. 2019, *MNRAS*, 488, L123
- Marinacci, F., Sales, L. V., Vogelsberger, M., Torrey, P., & Springel, V. 2019, *MNRAS*, 489, 4233
- Marques, L., Minchev, I., Ratcliffe, B., et al. 2025, *A&A*, 701, A88
- Martinez-Valpuesta, I. & Shlosman, I. 2004, *ApJ*, 613, L29
- Martinez-Valpuesta, I., Shlosman, I., & Heller, C. 2006, *ApJ*, 637, 214
- Merritt, D. 1996, *AJ*, 111, 2462
- Merritt, D. & Sellwood, J. A. 1994, *ApJ*, 425, 551
- Minchev, I. & Famaey, B. 2010, *ApJ*, 722, 112
- Moore, B., Ghigna, S., Governato, F., et al. 1999, *ApJ*, 524, L19
- Pfenniger, D. & Friedli, D. 1993, *A&A*, 270, 561
- Pillepich, A., Nelson, D., Hernquist, L., et al. 2018a, *MNRAS*, 475, 648
- Pillepich, A., Nelson, D., Springel, V., et al. 2019, *MNRAS*, 490, 3196
- Pillepich, A., Springel, V., Nelson, D., et al. 2018b, *MNRAS*, 473, 4077
- Power, C., Navarro, J. F., Jenkins, A., et al. 2003, *MNRAS*, 338, 14
- Quillen, A. C., Dougherty, J., Bagley, M. B., Minchev, I., & Comparetta, J. 2011, *MNRAS*, 417, 762
- Quillen, A. C., Minchev, I., Sharma, S., Qin, Y.-J., & Di Matteo, P. 2014, *MNRAS*, 437, 1284
- Raha, N., Sellwood, J. A., James, R. A., & Kahn, F. D. 1991, *Nature*, 352, 411
- Reddish, J., Kraljic, K., Petersen, M. S., et al. 2022, *MNRAS*, 512, 160
- Revaz, Y. & Jablonka, P. 2018, *A&A*, 616, A96
- Rodionov, S. A. & Sotnikova, N. Y. 2005, *Astronomy Reports*, 49, 470
- Romeo, A. B. 1994, *A&A*, 286, 799
- Romeo, A. B. 1997, *A&A*, 324, 523
- Romeo, A. B. 1998, *A&A*, 335, 922
- Romeo, A. B., Horellou, C., & Bergh, J. 2003, *MNRAS*, 342, 337
- Romeo, A. B., Horellou, C., & Bergh, J. 2004, *MNRAS*, 354, 1208
- Saha, K. & Elmegreen, B. 2018, *ApJ*, 858, 24
- Schaye, J., Crain, R. A., Bower, R. G., et al. 2015, *MNRAS*, 446, 521
- Sellwood, J. A. 2016, *ApJ*, 819, 92
- Semczuk, M., Lokas, E. L., & del Pino, A. 2017, *ApJ*, 834, 7
- Seo, W.-Y., Kim, W.-T., Kwak, S., et al. 2019, *ApJ*, 872, 5
- Springel, V., Di Matteo, T., & Hernquist, L. 2005, *MNRAS*, 361, 776
- Springel, V., Wang, J., Vogelsberger, M., et al. 2008, *MNRAS*, 391, 1685
- Steinmetz, M. & White, S. D. M. 1997, *MNRAS*, 288, 545
- Toomre, A. 1964, *ApJ*, 139, 1217
- Vislosky, E., Minchev, I., Khoperskov, S., et al. 2024, *MNRAS*, 528, 3576
- Weinberg, M. D. 1996, *ApJ*, 470, 715
- Weinberger, R., Springel, V., & Pakmor, R. 2020, *ApJS*, 248, 32
- White, R. L. 1988, *ApJ*, 330, 26
- Yurin, D. & Springel, V. 2014, *MNRAS*, 444, 62

Appendix A: Bar Strength without Smoothing

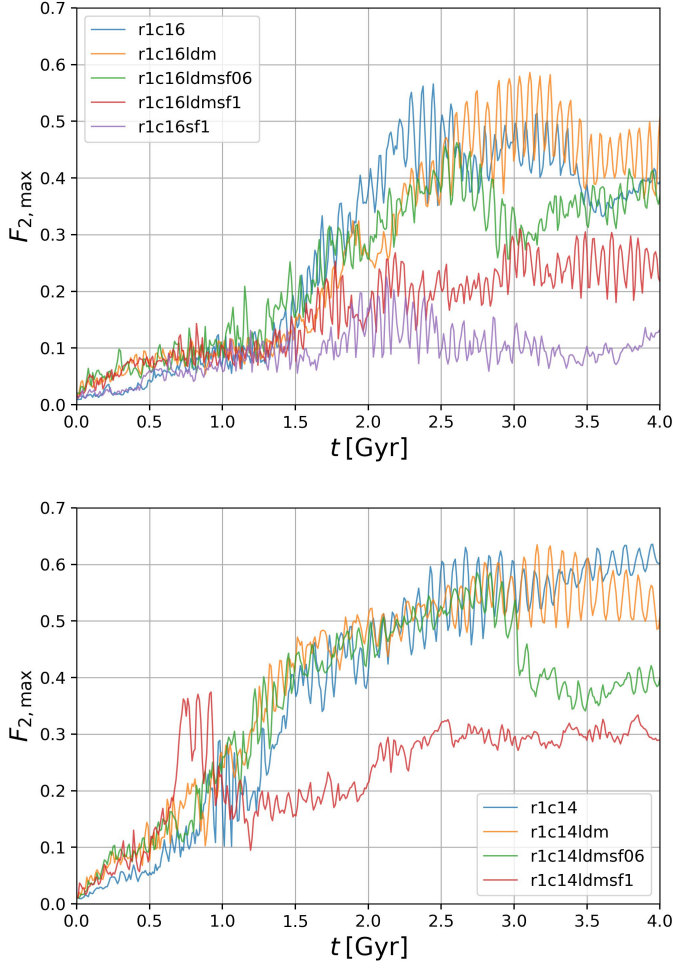


Fig. A.1: The same as Figure 4, but every snapshot with a timestep of 0.01 Gyr is shown without smoothing.

Appendix B: Additional Models

In addition to the nine models listed in Table 1, we construct two more models: r1c14hdm and r1c14ldmsf03. The ‘hdm’ designation indicates high DM resolution, adopting $m_{\text{DM}}/m_{\star} = 1$ with $N_{\text{DM}} = 1.14 \times 10^8$. In model r1c14, with different masses between DM and star particles, potential numerical effects could arise from using the same softening length for stars and DM particles (0.03 kpc). It turns out that such effects have a minimal impact on bar formation of unstable disks when comparing model r1c14 and r1c14hdm. For model r1c14ldmsf03, we test the effect of a DM softening length of 0.30 kpc to demonstrate the inverse correlation between the softening length and the buckling effects on bar strength.

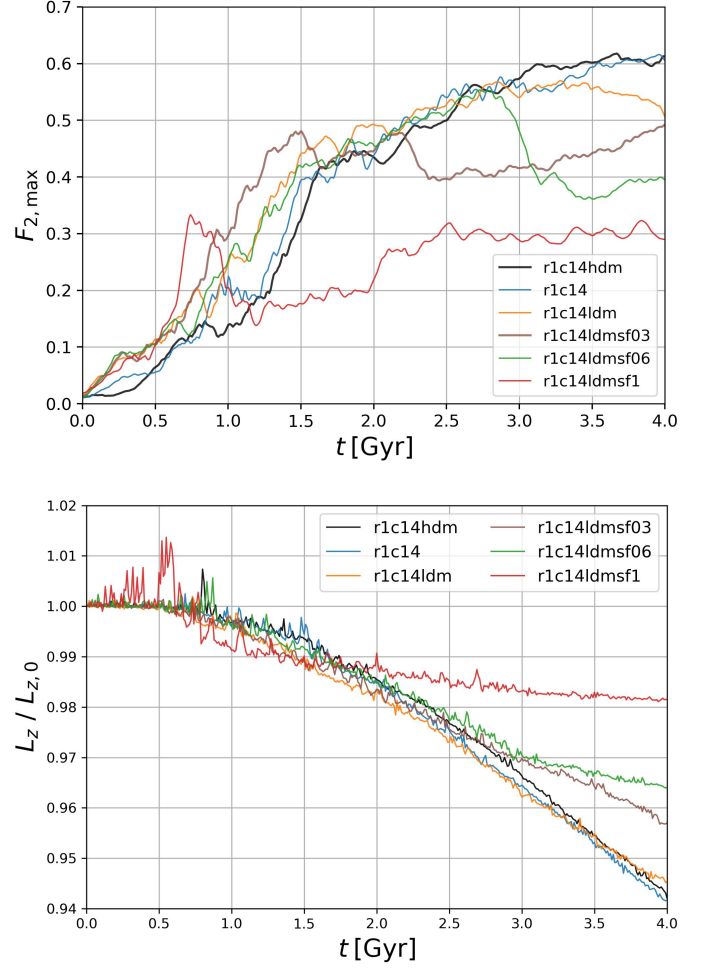


Fig. B.1: The same as Figure 4 and 5, but for the ‘c14’ models, additionally including models r1c14hdm ($m_{\text{DM}}/m_{\star} = 1$) and r1c14ldmsf03 ($\epsilon_{\text{DM}} = 0.30$ kpc).